Method for System-Level Multidisciplinary Uncertainty Analysis of Low-Boom Flight Vehicles

Christopher A. Eggert*, Laura M. White†, Joanna Schmidt‡, and Ben D. Phillips§
NASA Langley Research Center, Hampton, VA, 23666

Zachary D. Windous¶
Brigham Young University- Idaho, Rexburg, ID, 83460

Current research supporting NASA's Commercial Supersonic Technology project is focused on the efficient prediction of uncertainty in sonic boom loudness generated by low-boom aircraft concepts. This paper focuses on research incorporating aircraft trim and aerostructural analysis into a multidisciplinary system-level uncertainty analysis. This enables the modeling of a steady-state representation of a point in the uncertainty space, simulating the vehicle as it would be flown. This approach also enables multiple uncertain parameters defining the configuration of the vehicle to be reduced to three: Mach number, altitude, and aircraft weight. To demonstrate this methodology, a case study exploring a conceptual low-boom supersonic aircraft is performed. Two different approaches are used to model the interactions between nearfield pressure signature analysis and sonic boom propagation, and their performance is evaluated in terms of accuracy and computational expense. One method uses a set of local surrogate models to generate a large number of nearfield signatures and perform Monte Carlo analysis. This method is found to produce, at a lower expense, uncertainty metrics that are comparable to the second method, in which uncertainty metrics are computed based on loudness metric values obtained directly from simulated nearfield signatures.

Nomenclature

A_e	equivalent area	MSE	mean squared error
a	significance level	N_t	number of terms necessary for PCE model
d	PCE deterministic variables	n	PCE number of uncertain variables
C_L	lift coefficient	PCE	polynomial chaos expansion
C_{L_t}	target lift coefficient	p	pressure
C_{My}	pitching moment coefficient	p_{pce}	PCE order
C_{My_t}	target pitching moment coefficient	R	radius from aircraft centerline
C_D	drag coefficient	RSS	residual sum of squares
C_{D_t}	target drag coefficient	α	angle of attack
F	PCE response	$\Delta p/p_\infty$	nondimensional freestream pressure difference
F_a	F-distribution at significance level a	δ_{stab}	stabilator deflection angle
F_k	backwards elimination F-statistic	τ	nondimensional distance along signature
F_{out}	backwards elimination threshold	Ψ	PCE basis functions
h	altitude	$\boldsymbol{\xi}$	PCE random variables
M	Mach number		

I. Introduction

Over the past decade, there have been substantial investments in the development of computational tools for sonic boom prediction as well as low-boom vehicle design. More recently, research into methods of uncertainty quantification

*Aerospace Engineer, Aeronautics Systems Analysis Branch, Systems Analysis and Concepts Directorate
†Aerospace Engineer, Aeronautics Systems Analysis Branch, Systems Analysis and Concepts Directorate, Member AIAA.
‡Aerospace Engineer, Aeronautics Systems Analysis Branch, Systems Analysis and Concepts Directorate, Member AIAA.
§Aerospace Engineer, Aeronautics Systems Analysis Branch, Systems Analysis and Concepts Directorate, Member AIAA.
¶Visiting Professor, Department of Mechanical and Civil Engineering.

for vehicle analysis and design, as well as sonic boom prediction and mitigation, have been explored [1–9]. A current technical challenge for the NASA Commercial Supersonic Technology (CST) project is the development of tools to enable the integrated design of a low-boom aircraft. A crucial portion of this development is the consideration of uncertainties in the prediction of the perceived loudness on the ground [10]. The computation of aircraft sonic boom transmission to the ground starts with the estimation of pressure signatures in the nearfield, typically at a distance of three to five body lengths from the aircraft to ensure that three dimensional effects around the body are resolved. The nearfield pressure signatures are then propagated through the atmosphere. In this work, an approach numerically solving the augmented Burgers' equation [11] is applied. This procedure has two distinct areas where uncertainties are manifested: first in the measurement or simulation of nearfield pressure signatures, and second in the propagation parameter uncertainties, which are confounded by the nearfield uncertainties. Figure 1 depicts a schematic of the sonic boom computation and propagation process.

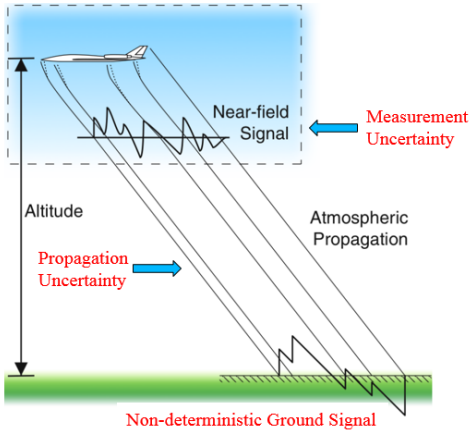

Fig. 1 Propagation of a pressure signature to the ground. [4, 12]

Previous research has been dedicated to the investigation of uncertainty in the prediction of low-boom aircraft signatures for implementation in certification procedures. West et al. [1, 2] have demonstrated efficient methods for certification prediction of low-boom aircraft. That work utilized a non-intrusive polynomial chaos approach in conjunction with novel dispersion methods outlined by Pinier [13] to place uncertainty bounds on both the nearfield pressure signatures and overall perceived noise levels on the ground. The work contributed to validation of nearfield pressure signatures generated by computational fluid dynamics (CFD) and sought to define a framework for certification prediction under uncertainty. Previous research conducted by Phillips and West [3] has shown that small changes in the outer mold line (OML) due to uncertainties in control surface deflections can have a significant impact on the overall uncertainty in ground noise. Phillips and West [6] also studied the impact of structural and aeroelastic uncertainties, which was an expansion on previous work by Nikbay et al. [5]. Both studies indicated that sensitivities to aeroelastic parameters account for a significant amount of overall predicted variance in ground noise and must be included in full system-level studies. Phillips et al. [9] first attempted to address the problem of trimming the model at each point within the uncertainty space with a focus on thrust-trimming. This was done by using throttle setting as the only design parameter while attempting to match the thrust and drag values for each data point. Results from this study indicated that variance and estimated uncertainty intervals of predicted ground noise can significantly increase when each point in the uncertainty model comes from a model at a steady state.

The objective of the current research is to develop a robust, system-level methodology for uncertainty quantification of low-boom aircraft configurations. This methodology utilizes a coupled framework incorporating aerodynamics, trim control, structural deformations, and grid adaptation to obtain nearfield pressure signatures. An uncertainty quantification case study is performed on a low-boom aircraft configuration, utilizing the coupled framework and two different methods for handling the interface between this framework and the subsequent boom propagation to the ground. The following section gives a brief overview of uncertainty quantification as it relates to sonic boom prediction and details the methods implemented in this research. Section III describes the case study and results produced using the newly developed approach, and concluding remarks are given in Section IV.

II. Methodology

This section is divided into two subsections. The first introduces the tools and methods employed in a system-level multidisciplinary analysis framework used to generate nearfield pressure signatures. The second focuses on uncertainty modeling methodology and describes the two methods for handling sonic boom uncertainty that are applied in this work.

A. Nearfield Pressure Signature Generation

Nearfield pressure signature generation is accomplished in a multidisciplinary analysis (MDA) framework, described in Fig. 2. A design of experiments (DOE) of desired sample points is fed into the system, from which the relevant trim targets and flow conditions are calculated. The flow solver is executed first and feeds its outputs into each of the other components. The outputs of the other disciplines are then routed back to the flow solver in the form of a surface grid modification. Once the MDA iteratively converges all relevant quantities, a final nearfield pressure signature is extracted. Later, in the boom propagation stage of the analysis, this signature is either propagated directly to the ground or is used in the creation of local surrogate models for indirect propagation.

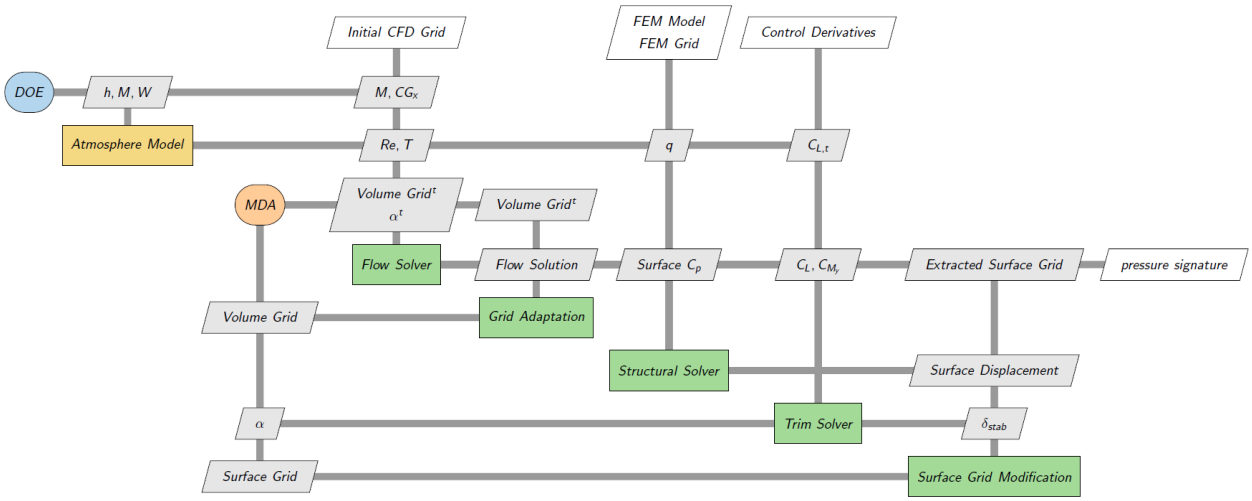

Fig. 2 MDA architecture for nearfield pressure waveform generation.

1. Flow Solver

The flow solver provides the required input information for all other components as well as computing the resultant nearfield pressure signature. Different solvers may be selected to achieve a desired balance of accuracy and computational cost. Codes solving either the Reynolds-averaged Navier-Stokes (RANS) or the Euler equations have been used to generate low-boom signatures. The second AIAA Sonic Boom Prediction Workshop [14] provides a good comparison between different solvers and approaches.

Although the methodology outlined here is adaptable to any CFD solver, this research used the Fully Unstructured Navier-Stokes Three-Dimensional (FUN3D) flow solver [15] due to its established history of prediction of nearfield sonic boom pressure waveforms [16, 17] and its widespread use across NASA. FUN3D is an unstructured node-based finite volume RANS code with the capability of solving both steady and unsteady laminar or turbulent flows for flight regimes ranging from subsonic to hypersonic. The flow solver uses a second-order accurate point-implicit method and allows accelerated convergence through scheduled ramping of the turbulent and meanflow Courant-Friedrichs-Lewy (CFL) conditions. The upwind inviscid scheme of Roe [18] is applied to compute cell interface fluxes, and the Spalart-Allmaras model [19] is coupled to the mean flow equations for turbulence closure. Nearfield signatures are generated by extracting nondimensional freestream pressure difference, $\Delta p/p_\infty$, data along a line sensor that has been aligned with the freestream flow by rotating to account for changes in angle of attack.

2. Grid Adaptation

After the initial CFD grid has been constructed, a feature-based grid adaptation package is executed once per MDA iteration to improve the nearfield pressure solution. This feature-based adaptation can produce grids of sufficient

resolution for signature extraction and was chosen over a goal-oriented adaptation package for its robustness and relative ease of implementation. Once the flow solver produces a flow solution on a given grid, error estimation is performed on the solution. The grid refinement package then adapts the grid to control interpolation error by placing nodes in regions of the flow domain with high gradient features. The number of MDA iterations depends on grid adaptation performance, since the grid adaptation process tends to be the limiting component of overall system convergence.

In this study, the *refine* grid refinement package built into FUN3D is used. This package is used to control the L_2 norm of interpolation error in the Mach field. This built-in version of *refine* cannot preserve the high aspect ratio cells needed near viscous surfaces, so the grid is frozen and left unadapted within a specified distance of viscous bodies (a nondimensional wall distance, y^+, of approximately 300). Each grid in the adaptation series is produced based on a target complexity (a value proportional to the number of nodes in the grid) to control grid size. In this work, 12 grid adaptation cycles, and therefore 12 total MDA iterations, were used to produce the nearfield pressure signatures for uncertainty quantification.

3. Static Aeroelastic Analysis

The research in this paper incorporates previously developed methods for determining static aeroelastic deformation. Only a brief overview is presented here; an in-depth discussion of the process can be found in previous works [5, 6]. The standalone estimation of a deformed vehicle shape as described in this section is integrated as one component of the broader MDA framework.

First, an initial CFD grid is generated on a jig shape geometry. A CFD solver is used to compute the pressure distribution on the aircraft, which is interpolated onto a finite element model (FEM) mesh. The pressure distribution is used as the loading condition for the static finite element analysis (FEA), from which structural nodal displacements are obtained. The displacements are passed back through the transfer scheme and applied to the CFD surface mesh. A grid deformation solver deforms the CFD surface and volume meshes, then the process is repeated until convergence in forces, moments, and displacements is reached.

Static aeroelastic analysis for this study is performed using Nastran [20], and FUNtoFEM [21] provides the transfer scheme between CFD and FEM grids. Deformation of the CFD volume grid is performed within FUN3D, using the GMRES algorithm [22] to solve a set of linear elasticity equations to recover the new, deformed surface grid.

4. Trim State Solver

A trim state solver ensures that a model state with balanced forces and moments is achieved for each sample within the uncertainty space. The solver uses estimated control derivatives with respect to angle of attack and control surface deflections. In this work, the derivatives were obtained from an initial CFD shape adjoint solution performed at the baseline flight conditions. The solver used in this work controls only the angle of attack, α, and the stabilator deflection angle, δ_{stab}, by solving the linear system shown in Eq. (1), where terms with subscript t indicate the target values. The target values for lift coefficient, C_L, and pitching moment coefficient, C_{My}, are derived from parameters such as current vehicle weight, altitude, and center-of-gravity (CG). The linear system is solved once per MDA iteration to produce the trim state of the aircraft. The trim state then converges along with the relevant forces and moments as a result of grid adaptation.

$$\begin{bmatrix} \frac{\partial C_L}{\partial \alpha} & \frac{\partial C_L}{\partial \delta_{\text{stab}}} \\ \frac{\partial C_{My}}{\partial \alpha} & \frac{\partial C_{My}}{\partial \delta_{\text{stab}}} \end{bmatrix} \begin{bmatrix} \alpha \\ \delta_{\text{stab}} \end{bmatrix} = \begin{bmatrix} -(C_L - C_{L_t}) \\ -(C_{My} - C_{My_t}) \end{bmatrix} \tag{1}$$

5. Farfield Propagation and Loudness Metrics

In order to propagate the nearfield signature through the atmosphere to the ground, the enhanced Burgers solver within PCBoom version 7.2.0 [23] is used. A sampling frequency of 120 kHz and a reflection factor of 1.9 are used for all cases in this work. Signatures are propagated through the atmosphere with uncertain perturbations applied to the x (streamwise) and y (spanwise) wind profiles, the temperature profile, and the humidity profile at all altitudes. For wind and temperature perturbations, a constant value is either added or subtracted from the baseline profile. For the humidity perturbation, the baseline humidity profile at all altitudes is multiplied by an uncertain humidity perturbation factor to obtain a new profile. The loudness metrics of interest are the B-, D-, and E-weighted sound exposure levels (BSEL, DSEL, and ESEL), as well as the Percieved Loudness in Decibels (PLdB), each of which represents a different

weighting of the audible frequency response. A review of previous studies done by Loubeau [24] determined that BSEL and DSEL are relatively robust metrics, whereas PLdB tends to be more sensitive to atmospheric effects and other sources of uncertainty.

B. Uncertainty Quantification Methodology

Uncertainty quantification (UQ) studies the impact of uncertainties in input parameters and modeling simplifications on the outputs of a process or simulation. UQ can vary in scope, from the inclusion of only a single model, to multiple models of varying fidelity, or to experimental data. The overarching goal of UQ is to create a more robust design or evaluation process by identifying sensitivities and mitigating the potential impact of uncertainties through informed, targeted resource investments. An important facet of UQ is the proper characterization and treatment of the simulation input uncertainties [4, 25], which can be grouped into two categories: aleatory and epistemic. Aleatory uncertainty refers to the inherent variability of a system, examples of which are atmospheric conditions such as humidity, temperature, and wind. Epistemic uncertainty refers to uncertainty derived from a lack of knowledge about the behavior of the system and can be reduced with more information. Examples of model input epistemic uncertainties in the analysis of boom signatures include the ground elevation and reflection factor. To perform a UQ study for sonic boom generation and propagation, multiple methods are necessary.

Two different methods are applied to handle the interface between nearfield pressure signature generation and farfield sonic boom prediction: direct propagation and indirect propagation. Direct propagation passes the nearfield signatures from CFD directly to the propagation code, producing loudness values that can be used to fit a polynomial chaos expansion (PCE) surrogate model and perform UQ. Alternatively, indirect propagation involves first converting the CFD signatures to equivalent area distributions, then generating a set of local PCE models at discrete points along the equivalent area curves, and finally using those PCE models to generate and propagate new signatures at sample points throughout the the uncertainty space. The indirect method has the advantage of requiring fewer CFD runs, due to the reduced number of uncertain parameters used to fit the local PCE models. Regardless of which method is used, the final step in the UQ process is to characterize the overall uncertainty through Monte Carlo analysis. The following three sections will give a brief review of the specific UQ methods adapted for this work.

1. Second-Order Probability

To propagate uncertainty through the model, the second-order probability approach, outlined by Eldred and Swiler [26] for the treatment of mixed aleatory and epistemic uncertainties, is employed. A flowchart of the method is shown in Fig. 3a. In this application, the black-box simulation is either the combined nearfield signature MDA and farfield sonic boom prediction or a surrogate model of that process.

For each sample of the set of epistemic uncertain parameters, a cumulative distribution function (CDF) can be generated from the set of associated aleatory uncertainties as seen in Fig. 3b. The probability box (P-Box) plot shows the family of CDFs generated from the second-order probability approach. To determine a 95% uncertainty interval on the perceived ground noise, the lowest perceived noise level extracted from a CDF at the 2.5% probability level and the highest perceived noise level extracted from a CDF at the 97.5% probability level are chosen (for a significance level a=0.05). The use of the P-Box uncertainty approach is conservative, but it is statistically justifiable for the given inputs to the simulations. Note that the choice of significance level is somewhat subjective and can alter the findings. A lower value of a is more conservative and will produce wider uncertainty intervals.

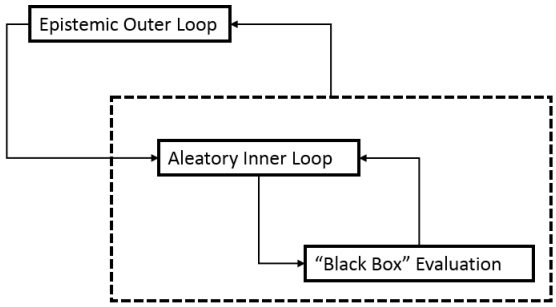

(a) Each iteration of the epistemic outer loop represents one sample of the epistemic uncertain variables.

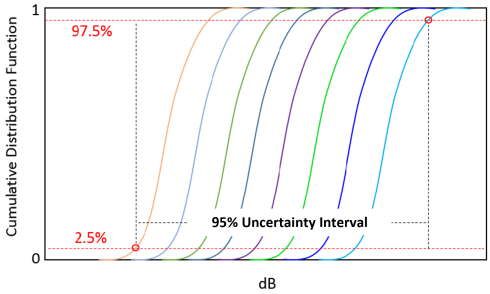

(b) Each CDF shown in this P-Box plot is generated within the aleatory inner loop, and represents one iteration of the epistemic outer loop.

Fig. 3 The second-order probability architecture.

2. Point-Collocation Non-Intrusive Polynomial Chaos

A second method utilized in this research is non-intrusive polynomial chaos with point-collocation. Compared to traditional sampling methods such as Monte Carlo, the polynomial chaos method has been demonstrated as a viable and economical means of uncertainty quantification for CFD-based applications [27]. Polynomial chaos is a surrogate modeling technique based on a spectral representation of uncertainty. An important aspect of such a representation is that a response value or random function, F, can be decomposed into separable deterministic and stochastic components, as shown in Eq. (2).

$$F(\boldsymbol{d}, \boldsymbol{\xi}) \approx \sum_{i=0}^{P} A_i(\boldsymbol{d}) \Psi_i(\boldsymbol{\xi}) \tag{2}$$

Here, A_i is the deterministic component and Ψ_i is the random variable basis function corresponding to the i^{th} mode. The basis function, Ψ_i, of each random variable is determined using the Askey scheme [28] and is dependent on the distribution of the random variable. The response, F, is a function of independent, random variables, $\boldsymbol{\xi}$, and deterministic variables, $\boldsymbol{d}$. This infinite series is truncated in practice. To form a complete basis, N_t terms are required, which can be computed from Eq. (3) for a PCE of order p_{pce} and a number of random dimensions or variables n. Further details on polynomial chaos theory are given by Ghanem [29] and Eldred [30].

$$N_t = \frac{(n + p_{\text{pce}})!}{n! p_{\text{pce}}!} \tag{3}$$

To compute the expansion coefficients, A, the non-intrusive point-collocation method is utilized [27]. The response F is sampled at locations throughout the random variable space, and the expansion coefficients are computed with an over-determined, least squares approach. At least N_t samples are needed for this procedure; Hosder et al. [27] recommend an oversampling ratio of two (i.e., $2 \cdot N_t$ samples). A Latin hypercube sampling (LHS) approach is used to ensure coverage of the domain spanned by the random variables, sometimes augmented by other DOE formats, such as a fractional factorial DOE to sample the corners of the uncertainty space. Once the PCE expression in Eq. (2) is obtained, analytical expressions for the mean and standard deviation of F are available [30], as are Sobol indices (global nonlinear sensitivity parameters) [31]. Alternatively, Monte Carlo sampling of the low-cost PCE may be conducted in order to obtain probability density functions (PDF), higher order moments, probabilities of failure, etc.

3. Backwards Elimination with Polynomial Chaos Expansion

Backwards elimination is the process of removing the model terms that are the least significant within the PCE model; it helps to remove noise in the model by reducing overfitting. For this work, the methods described by Montgomery et al. [32] are applied to determine which terms can be eliminated from the PCE model.

The method starts by building a full PCE model, then removing effects one-by-one until a stopping condition has been satisfied. At each iteration, the term with the smallest contribution to the model is discarded. Backwards

elimination uses a partial F-distributed variable to determine whether a term will be removed from the model, which is shown in Eq. (4).

$$F_{\text{out}} = F_a(d_1 = 1, d_2 = N - p_{\text{iter}}) \tag{4}$$

Here, F_a is an F-distribution at significance level a, N is the number of samples used to build the PCE model, and p_{iter} is the current number of terms used in the model. A value of $a = 0.1$ was found to produce the best PCE model fit for datasets in this study, screening roughly half of the PCE model terms out. F_{out} represents the threshold used to determine whether a term in the model is kept or discarded. To calculate the effect of a term on a model, the ratio of the residual sum of squares (RSS) with one term deleted to the mean squared error with all model terms is calculated, as shown in Eq. (5).

$$F_k = \frac{RSS_{p_{\text{iter}}-k} - RSS_{p_{\text{iter}}}}{MSE/(N - p_{\text{iter}})} \tag{5}$$

Here, $RSS_{p_{\text{iter}}-k}$ is the residual sum of squares with the kth term removed from the model for $k \in \{1, \ldots, p_{\text{iter}}\}$, $RSS_{p_{\text{iter}}}$ is the residual sum of squares for the full model, and MSE is the mean squared error of the full model. Note that for Eq. (5), the intercept term is always included in the model (i.e. $k \neq 0$). The following steps define the complete backwards elimination process:

1. Build the PCE model on p_{iter} terms.
2. Calculate F_k for each term in the model using Eq. (5).
3. If $\min_{k \in \{1,\ldots,p_{\text{iter}}\}} F_k < F_{\text{out}}$, delete the term corresponding to the minimum F-statistic from the PCE model.
4. Set $p_{\text{iter}} = p_{\text{iter}} - 1$.
5. Repeat steps 1-4 until $F_k \geq F_{\text{out}}$ for all $k \in \{1, \ldots, p_{\text{iter}}\}$.

4. Uncertainty Quantification with Polynomial Chaos Expansion (UQPCE)

All of the uncertainty modeling and analysis contained in this research is performed using Uncertainty Quantification with Polynomial Chaos Expansion, UQPCE [33]. UQPCE is an open source, Python-based research code for use in parametric, non-deterministic computational analysis and design. UQPCE utilizes a non-intrusive polynomial chaos expansion surrogate modeling technique (see Section II.B.2) to efficiently estimate uncertainties for computational analyses. The software enables the user to perform an uncertainty analysis for any given computational code without requiring modification to the source. UQPCE estimates sensitivities, uncertainty intervals, and other model statistics which can be useful in the conceptual design and analysis of flight vehicles. This software was developed to study potential impacts of uncertainties on the prediction of ground noise generated from commercial supersonic aircraft concepts.

5. Quasi-Monte Carlo Variance Analysis

A Sobol sensitivity index method was employed to assess the sensitivity of the loudness metrics to the uncertain input parameters. The Sobol sensitivity index, a variance-based method for performing global sensitivity analysis that uses variance as the basis for quantifying the influence of each input parameter on overall output variation, was chosen for this analysis [34]. This method was selected due to its compatibility with Monte Carlo methods.

The total-effect Sobol index, S_{T_i}, is given in Eq. (6), which measures the contribution of the output variance of parameter X_i including all the variance caused by interactions with other parameters.

$$S_{T_i} = \frac{\mathbb{E}_{\sim i}[\mathbb{V}_i[\mathbf{Y}|\mathbf{X}_{\sim i}]]}{\mathbb{V}[\mathbf{Y}]} \tag{6}$$

In this equation, $\mathbb{E}_{\sim i}[\mathbb{V}_i[\mathbf{Y}|\mathbf{X}_{\sim i}]]$ represents the expected value of the remaining variation in the output $\mathbf{Y}$ when all parameters are fixed except $\mathbf{X}_i$. For this work, a quasi-Monte Carlo method is applied, following the approach outlined by Saltelli et al. [35]. This approach replaces random sequences with low-discrepancy sequences, enhancing the efficiency of the Sobol index estimators.

6. Direct and Indirect Propagation Methods

As described above, the computation of sonic boom ground loudness metrics involves two phases. In the first phase, a CFD solver is used to compute the nearfield pressure signature. The second phase entails solving an augmented

Burgers' equation to propagate the nearfield signature through the atmosphere, resulting in a farfield waveform and the ground loudness metrics. The handling of the interface between the two phases presents challenges to UQ methods, but it also offers an opportunity to reduce the computation cost of performing UQ. This work employs two different methods for handling this interface: the direct propagation method and the indirect propagation method. Both will be described here and are diagramed in Fig. 4.

For direct propagation, each nearfield signature from the flow solver is fed directly into PCBoom, along with the values of the uncertain parameters that were used to generate that signature. In this way, both the system-level MDA and PCBoom receive the same values for any shared parameters, and no connecting information is lost. Using direct propagation, the same number of samples of each loudness metric will be produced as the number of times the nearfield MDA is executed, meaning that each loudness metric sample is very expensive. For the eight uncertain parameters in the case study below, ninety MDA runs were required to build the PCE model using direct propagation.

The indirect propagation method involves separating the nearfield signature generation phase from the farfield propagation phase. This is done by taking the set of nearfield pressure signatures obtained via CFD simulation and using them to fit surrogate models and generate large quantities of surrogate-generated pressure signatures, instead of feeding them directly to the propagation code. Crucially, indirect propagation can be much cheaper than direct propagation because instead of creating the signature surrogate models based on the full set of uncertain parameters, only the subset of uncertain parameters related to the nearfield is used. Since the number of samples required to fit a model tends to increase quickly with the number of input parameters, this distinction represents a large reduction in the overall computation expense of a UQ study. In the case study below, only twenty-one MDA runs were required using this method.

Previous research [1–3, 5] has utilized a Fourier dispersion method developed by Pinier [13] to accomplish indirect propagation. This method generates nearfield signatures randomly within a range of lower and upper $\Delta p/p_\infty$ bounds. Although it is efficient and produces realistic nearfield signatures, one limitation is that it does not establish a direct connection between each new signature and any specific values of the input uncertain parameters. Since some parameters are often shared between the nearfield and propagation phases, having a way to associate these values with a specific signature can preserve the connection between the nearfield and propagation phases.

In the case study below, indirect propagation is implemented through the construction of a series of local PCE models along the length of the nearfield signatures. Each model is fit based on the nearfield subset of uncertain parameters (i.e., Mach number, altitude, and weight) and therefore maintains the connection between the model outputs and those input parameters. Instead of fitting the local PCE models to the $\Delta p/p_\infty$ curves obtained directly from CFD solutions, each CFD signature is first converted to its equivalent area (A_e) representation, which creates a smooth curve without discontinuities at the shock locations. These smooth curves result in PCE model fits of much higher quality, while still retaining all necessary information. After the local PCE models are constructed, they can be sampled at new values of Mach number, altitude, and weight to quickly generate new A_e curves, which can then be converted back to $\Delta p/p_\infty$ nearfield pressure signatures for use in Monte Carlo analysis. For details on how the conversion between equivalent area and pressure along the nearfield is performed, refer to Rallabhandi [36].

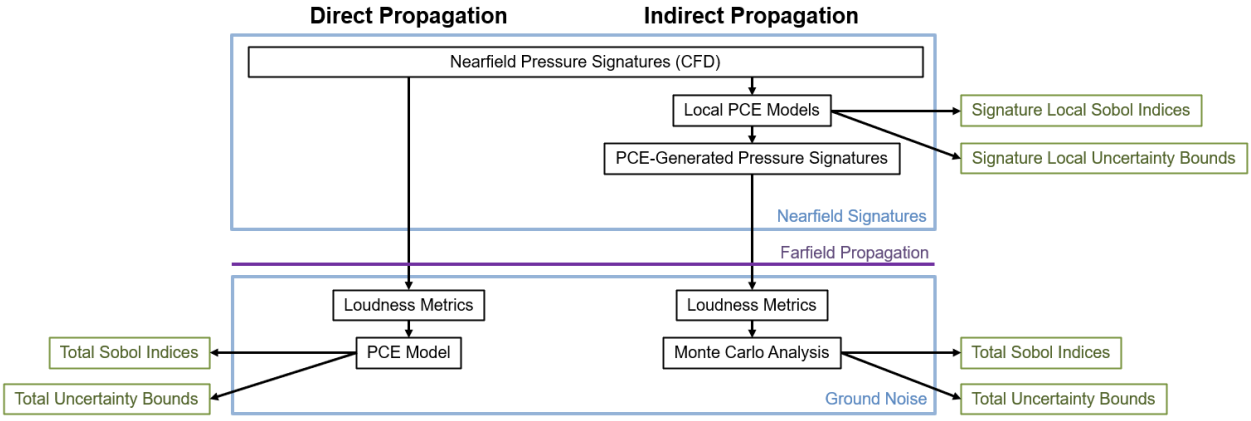

Fig. 4 Comparison of direct and indirect propagation methods for the computation of uncertainty metrics.

III. Case Study

This section begins with an overview of the computational setup used in this case study, followed by a description of the various numerical models, evaluations of their convergence, and results from the uncertainty models.

A. Computational Setup

To demonstrate the system-level uncertainty quantification methodology outlined in Section II.A, the NASA C25P supersonic aircraft concept is modeled. This aircraft has been optimized to reduce the undertrack sonic boom with propulsive boundary conditions at the engine faces activated [37, 38]. It has also been included in CFD studies such as the second AIAA Sonic Boom Prediction Workshop [14]. The geometry used in this study includes left and right stabilators that are separated from the rest of the aircraft body to allow them to rotate independently of the aircraft body. The aircraft and stabilator geometries are shown in Fig. 5.

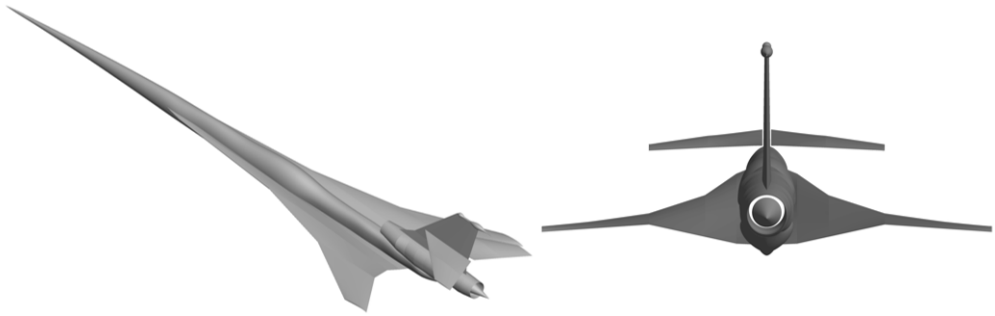

Fig. 5 C25P Geometry, with separated stabilators.

An initial cruise point of Mach 1.60, altitude of 51,314 ft, angle of attack of 3.375°, and weight of 21,000 lb is analyzed as the baseline condition. Before the iterative MDA process begins, a target C_L is computed based on the aircraft weight, altitude, and Mach number. A target C_{My} is also included but is always set to zero as computed based on a fixed moment reference point; a fixed center of gravity at $x = 79.7$ ft is assumed due to the tight control of the location of the center of gravity in supersonic aircraft. The trim solver, described in Section (II.A.4), is set up to adjust α and δ_{stab} to match these computed values of C_{L_t} and C_{My_t}.

Recall that each MDA iteration contains an FEA run, surface and volume grid deformation, and volume grid adaptation as discussed in Sections II.A.2 and II.A.3.

1. FEM Model

The FEM model is based on a triangulation of the C25P wing and empennage geometry generated using OpenVSP [39] and appropriately converted within MSC Patran [40]. It represents the wing structure as a hollow shell and consists of 4,127 nodes and 8,242 triangular elements. The boundary conditions are set to simulate a cantilever wing, for which nodes at the junction between the wing and fuselage are fixed, allowing no translation or rotation. Initial sizing of the shell element thickness was done to create a nominal tip displacement of approximately 1.5 inches at the baseline flow conditions. Structural analysis for the case study is completed within MSC Nastran [20]. It is worth noting that since the unloaded FEM grid was built based on the design cruise shape of the C25P, aeroelastic analysis will not yield the design shape, but instead a shape with the wings deflected slightly upwards. Although not as true to the design of the C25P as deforming from a jig shape geometry would be, the evaluation of overall uncertainty analysis methods is still possible with this setup. The finite element grid is shown in Fig. 6 with typical wingtip displacements overlayed.

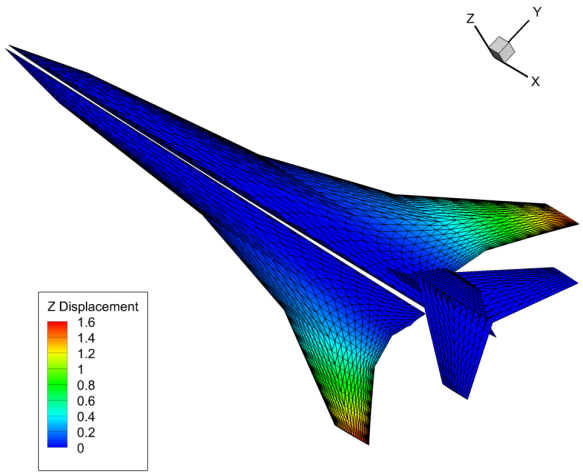

Fig. 6 C25P finite element grid, with typical converged displacements.

The aerostructural problem converges within the MDA process. Baseline convergence can be seen in Fig. 7, where wingtip displacement of the left wing is shown. Wingtip displacements of around 1.6 inches are typical, with the value converging to within 0.01 inches by MDA iteration 12.

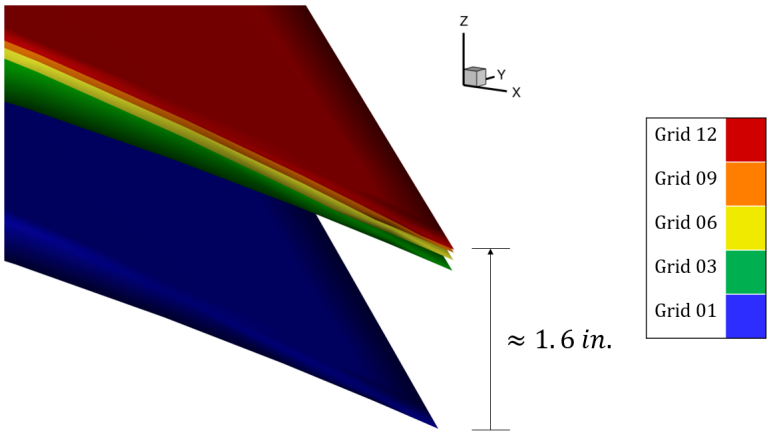

Fig. 7 C25P aerostructural convergence of displacement at the left wingtip.

2. CFD Model

The initial CFD grid was constructed using the Heldenmesh suite of grid generation tools [41] around the C25P geometry, with the outer flow domain boundary in a conical boom-grid shape. The FUN3D flow solver and its built-in *refine* grid adaptation library are used to iteratively resolve the nearfield signature for 12 cycles. The initial grid contains 200,000 surface nodes and 7.3 million volume nodes, whereas the adapted, converged grids contain approximately 36 million volume nodes. Baseline grid adaptation is shown in Fig. 8, and signature convergence through the 12 adaptation cycles is shown in Fig. 9. All nearfield signatures for this case study are undertrack signatures taken directly beneath the aircraft geometry at a distance of three body lengths.

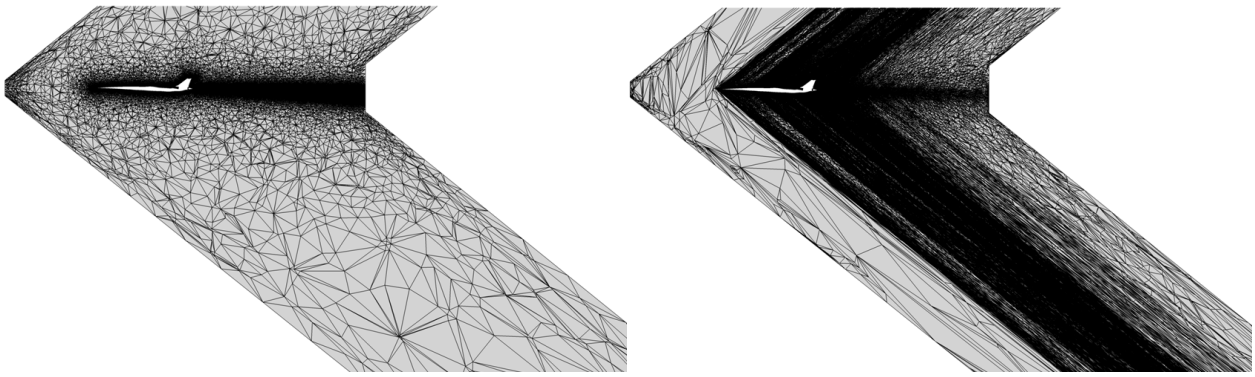

(a) Initial, Grid 1. (b) Adapted, Grid 12.

Fig. 8 Feature-based grid adaptation performed using FUN3D's built-in *refine* package.

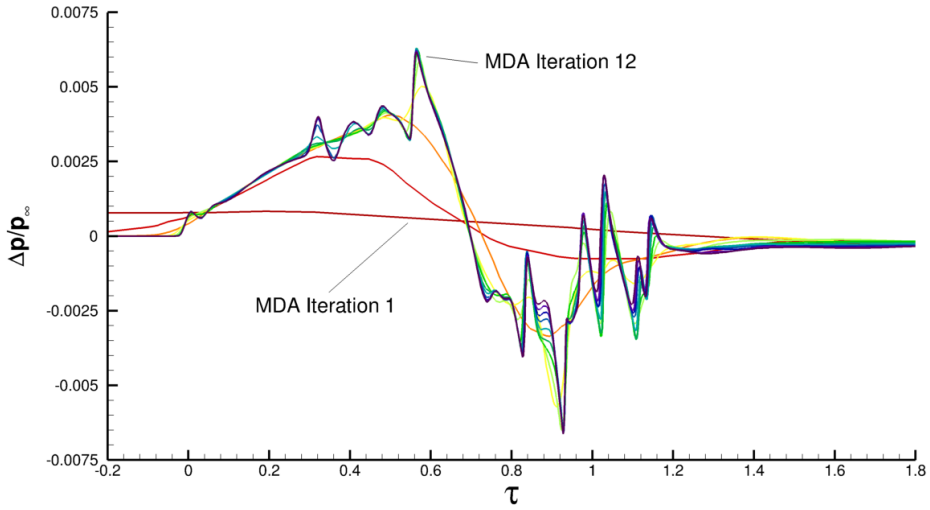

Fig. 9 Nearfield pressure signature shape convergence with grid adaptation.

Convergence histories of loudness metrics and trim variables are shown in Fig. 10. Angle of attack converges to within 0.01 degrees by MDA iteration 12. The stabilator deflection angle, for which changes are based on the changes in integrated pitching moment of the flow solution as the grid is adapted, converges much more slowly but still to within 0.025 degrees. Of the loudness metrics, three converge to within 0.1 dB by MDA iteration 12: BSEL, DSEL, and ESEL. The fourth metric, PLdB, converges less reliably to within approximately 0.4 dB. This is a limitation of the PLdB metric, which is less robust than the other three.

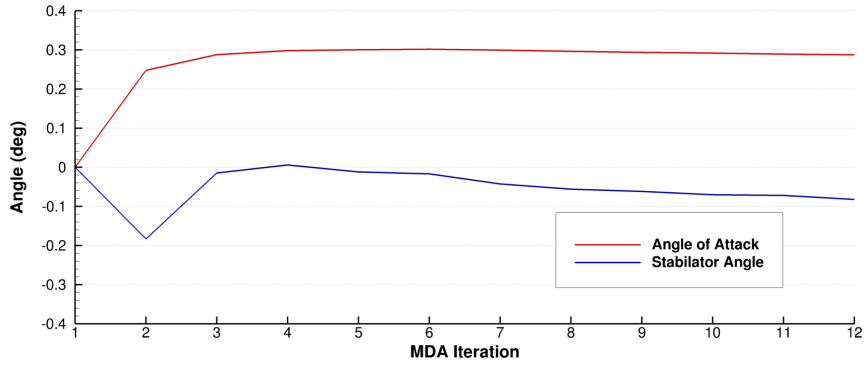

(a) Trim variable changes from starting conditions.

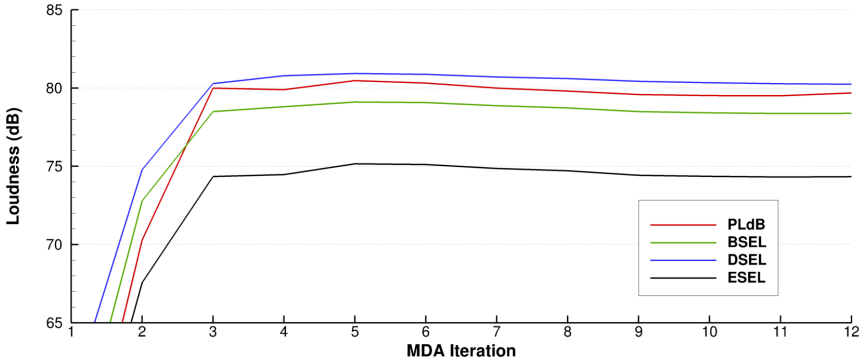

(b) Loudness metrics.

Fig. 10 Convergence of loudness metrics and trim variables throughout the MDA process, for the baseline case.

B. Uncertainty Modeling

Three uncertain nearfield parameters are modeled in this case study: Mach number, altitude, and weight. In addition, five uncertain propagation parameters are included: ground altitude, perturbations of wind in the x-direction and y-direction, perturbation in temperature, and a humidity factor. Their treatment and distributions are given in Tables 1 and 2. The values of the various distributions are chosen based on historical estimates such as values found in Ref. [1], and from NASA X-59 flight simulator data, adjusted to suit the C25P flight conditions. Atmospheric perturbations are applied to a standard atmosphere with no wind as was used in the sonic boom prediction workshop [14]; wind and temperature perturbations are added to their baseline values across all altitudes, whereas the standard humidity profile is multiplied by the uncertain humidity factor to obtain a profile.

Table 1 Uncertain Input Parameters, Nearfield

Input	Type	Distribution	Distribution Definition	Units
Mach Number	Epistemic	Interval	[1.58, 1.62]	-
Altitude	Epistemic	Interval	[50,407.5, 52,992.5]	ft
Weight	Epistemic	Interval	[19,950.0, 22,050.0]	lbf

Table 2 Uncertain Input Parameters, Propagation

Input	Type	Distribution	Distribution Definition	Units
Mach Number	Epistemic	Interval	[1.58, 1.62]	-
Altitude	Epistemic	Interval	[50,407.5, 52,992.5]	ft
Ground Altitude	Epistemic	Interval	[600, 1,400]	ft
X-Wind Perturbation	Aleatory	Normal	$\mathcal{N}(0,4)$	ft/s
Y-Wind Perturbation	Aleatory	Normal	$\mathcal{N}(0,4)$	ft/s
Temperature Perturbation	Aleatory	Normal	$\mathcal{N}(0,3)$	$^\circ F$
Humidity Factor	Aleatory	Normal	$\mathcal{N}(1.0,0.05)$	-

Note that Mach number and altitude appear in both tables, because they play a role in both nearfield signature generation and farfield signature propagation. For UQ performed using direct propagation of the nearfield samples to the ground, instances of these parameters in the nearfield phase are coupled to instances in the propagation phase, so that they hold the same values throughout the analysis. For indirect propagation through the use of local PCE models, these parameters are coupled via the training of each local PCE model.

For direct propagation UQ, a second-order PCE model requires 90 total runs to achieve a nominal oversampling ratio of 2. The full DOE is constructed by combining a fractional factorial DOE with LHS DOE to achieve the required total. This design provides good coverage of the uncertainty space both at its corners and in its interior. Additional verification runs are also obtained via an additional LHS DOE. The fit metrics for the PCE model after backwards elimination has been performed are shown in Table 3. These metrics reflect the fact that BSEL and DSEL converge more reliably during the MDA process than PLdB, and are therefore easier to fit a PCE model to.

Table 3 PCE Model Fit Metrics, Direct Propagation

Metric	PLdB	BSEL	DSEL	ESEL
R^2	0.858	0.947	0.982	0.862
Mean Model Error (dB)	0.20	0.10	0.05	0.14
Mean Verification Error (dB)	0.31	0.15	0.06	0.17
Max Verification Error (dB)	0.57	0.31	0.12	0.33

Total Sobol indices generated within UQPCE are shown in Table 4 and Fig. 11. All loudness metrics are most sensitive to uncertainty in aircraft weight and altitude, with DSEL being the metric most sensitive to weight and PLdB the most sensitive to altitude. Since weight and altitude determine the target lift coefficient, they also determine the aircraft angle of attack and stabilator angle via the trim solver. The angle of attack and stabilator then have a large effect on the shape of the nearfield pressure signature and, therefore, on the ground loudness metrics. Sensitivities to Mach number, x-wind perturbation, temperature perturbation, and humidity factor are also present to varying degrees in the loudness metrics. The y-wind perturbation terms, on the other hand, are insignificant and eliminated from all four PCE models during backwards elimination.

Table 4 Sobol Indices, Direct Propagation

Input	PLdB Sobol	BSEL Sobol	DSEL Sobol	ESEL Sobol
Mach Number	0.065	0.056	0.030	0.090
Altitude	0.416	0.221	0.130	0.273
Weight	0.370	0.652	0.774	0.480
Ground Altitude	0.022	0.021	0.000	0.036
X-Wind Perturbation	0.146	0.067	0.000	0.030
Y-Wind Perturbation	0.000	0.000	0.000	0.000
Temperature Perturbation	0.163	0.086	0.084	0.170
Humidity Factor	0.109	0.032	0.017	0.107

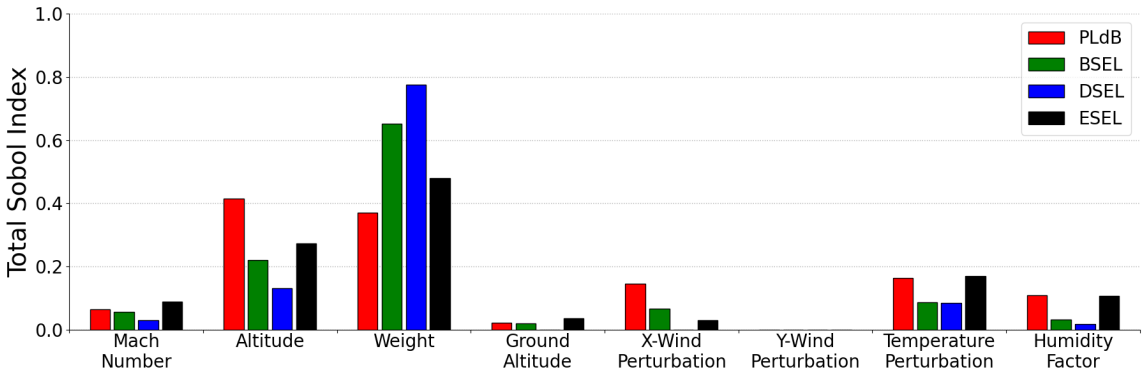

Fig. 11 Loudness metric uncertainty sensitivities from the direct propagation method.

For indirect propagation, only 21 MDA runs are used to build all of the local PCE models across the length of the signatures, since those local PCE models are only dependent on the nearfield set of uncertain variables. 3,600 local PCE models are constructed at points across the length of the signatures. Verification cases are used to characterize the error in loudness metrics resulting from the A_e conversion process and local PCE fitting. These cases compare metrics obtained by running PCBoom on a CFD pressure signature to those obtained by running on a PCE-generated signature from the matching location in the uncertainty space. PCE-generated signatures are shown to be slightly quieter on average for all loudness metrics, indicating that a small amount of signature content is lost as a result of the processing and modeling. The average decreases in loudness between CFD signatures and PCE-generated signatures are 0.11 dB for PLdB, 0.08 dB for BSEL, 0.03 dB for DSEL, and 0.11 dB for ESEL. Fit metrics for loudness values computed using PCE-generated signatures are found in Table 5.

Table 5 PCE Model Fit Metrics, Indirect Propagation

Metric	PLdB	BSEL	DSEL	ESEL
R^2	0.948	0.966	0.983	0.958
Mean Model Error (dB)	0.13	0.09	0.04	0.09
Mean Verification Error (dB)	0.19	0.12	0.05	0.14
Max Verification Error (dB)	0.55	0.37	0.17	0.43

For this study, 36 million PCE-generated signatures are then generated and propagated to collect statistics and perform UQ via quasi-Monte Carlo analysis. This equates to 6 million base Monte Carlo samples to determine the

uncertainty bounds, plus 30 million additional samples in order to capture the total Sobol indices through variance analysis as described in Section II.B.5. Results from this method are shown in Table 6 and Fig. 12. A comparison between the total Sobol indices obtained via the direct and indirect propagation methods shows good agreement for the BSEL and DSEL metrics. For PLdB and ESEL, the two methods still produce similar trends in Sobol index values, but there is poorer agreement. This is likely due to error within the PCE models for these metrics, which may be caused by either noise from remaining grid error in the flow solution or by higher order effects not captured by second-order PCE fits.

Table 6 Sobol Indices, Indirect Propagation

Input	PLdB Sobol	BSEL Sobol	DSEL Sobol	ESEL Sobol
Mach Number	0.077	0.057	0.028	0.082
Altitude	0.743	0.313	0.151	0.575
Weight	0.225	0.722	0.801	0.268
Ground Altitude	0.004	0.001	<0.001	0.007
X-Wind Perturbation	<0.001	<0.001	<0.001	<0.001
Y-Wind Perturbation	0.007	0.003	0.002	0.010
Temperature Perturbation	0.074	0.058	0.066	0.074
Humidity Factor	0.109	0.048	0.022	0.136

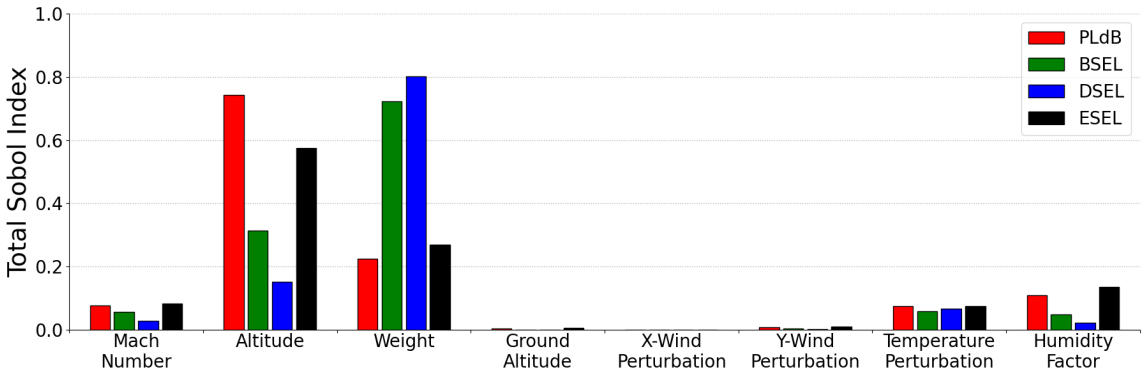

Fig. 12 Loudness metric uncertainty sensitivities from the indirect propagation method.

Finally, 95% uncertainty intervals are produced for each metric and method, as shown in Table 7 and in Fig. 13 along with the mean values of each metric. The two methods show good agreement in both predicted mean and in uncertainty interval bounds for all metrics. Again, the agreement is weakest for PLdB and strongest for DSEL. The mean values predicted using the indirect method are slightly lower than those predicted using the direct method for all metrics, which is in line with average loudness metric discrepencies present in the local PCE verification cases.

Table 7 95% Uncertainty Intervals

Loudness Metric	Direct Propagation	Indirect Propagation
PLdB	[77.93, 81.26]	[78.42, 81.41]
BSEL	[77.35, 80.24]	[77.70, 80.30]
DSEL	[79.70, 81.64]	[79.65, 81.59]
ESEL	[73.33, 75.66]	[73.58, 75.67]

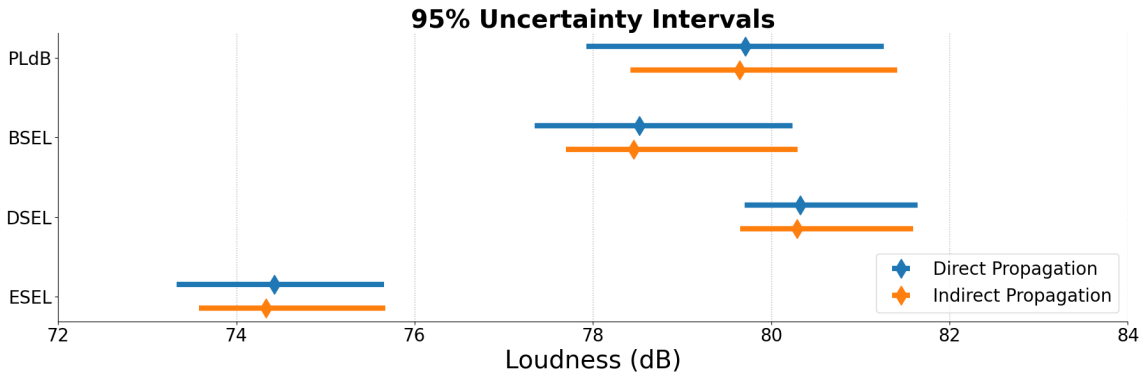

Fig. 13 95% uncertainty intervals for direct and indirect propagation.

Table 8 provides a brief overview of the computational expense incurred by each method during this case study. All computations are performed in parallel on 400 cores. Each full MDA execution takes approximately 11.6 hours, and the Monte Carlo executions can be completed at a rate of 600,000 per hour. For this case study, the cost of performing UQ using the indirect propagation method is approximately 30% of the cost using the direct method. That advantage decreases as the cost of each MDA is reduced, and vice versa.

Table 8 Computational Expense Comparison

	Direct Propagation	**Indirect Propagation**
MDA Executions	90	21
Monte Carlo Executions	–	36,000,000
MDA Wall Time (hrs)	1047	244
Monte Carlo Wall Time (hrs)	–	60
Total Wall Time (hrs)	1047	304

IV. Conclusions

An MDA framework for simulating low-boom conceptual aircraft designs at the system level is created and examined on a UQ case study of the NASA C25P aircraft concept. The framework generates nearfield pressure signatures using the FUN3D RANS flow solver and successfully incorporates both aeroelastic and trim effects through the use of Nastran FEA and a trim solver. The case study shows that some loudness metrics converge more quickly than others within the MDA framework; BSEL and DSEL converge easily, whereas PLdB is more sensitive to the remaining grid and trim error. Two methods for linking the nearfield simulation to the PCBoom sonic boom propagation code are also considered and compared: the direct method, in which the signatures extracted from the flow solution are fed directly to PCBoom, and the less computationally expensive indirect method, in which a series of local PCE models is fit to those signatures and used to produce large quantities of surrogate-generated signatures for Monte Carlo analysis. Uncertainty metrics such as the 95% uncertainty interval bounds and the total Sobol indices computed using these two methods agree fairly well. Trends in uncertainty sensivities agree very well for the BSEL and DSEL loudness metrics. Trends in sensitivities for PLdB and ESEL roughly match between the two methods, and differences may be attributed to surrogate modeling error. The indirect propagation method with local PCE models, although more complex to implement, maintains linkage of information between the nearfield and propagation steps and can substantially reduce the computational expense of an uncertainty study while producing comparable uncertainty estimates.

Future work could extend or improve various pieces of the MDA framework, such as by creating a more realistic structural model or by incorporating propulsion uncertainty into the nearfield signature generation process. The methods in this paper could also be applied to other low-boom aircraft configurations, or to a full sonic boom carpet instead of only undertrack sonic boom loudness.

References

[1] West IV, T. K., Reuter, B. W., Walker, E. L., Kleb, B., and Park, M. A., "Uncertainty Quantification and Certification Prediction of Low-Boom Supersonic Aircraft Configurations," *Journal of Aircraft*, Vol. 54, No. 1, 2017, pp. 40–53. https://doi.org/10.2514/1.C033907.

[2] West IV, T. K., Bretl, K., Walker, E., and Pinier, J. T., "Sonic Boom Pressure Signature Uncertainty Calculation and Propagation to Ground Noise (Invited)," AIAA Paper 2015-1251, January 2015. https://doi.org/10.2514/6.2015-1251.

[3] Phillips, B. D., and West IV, T. K., "Trim Flight Conditions for a Low-Boom Aircraft Under Uncertainty," *Journal of Aircraft*, Vol. 56, No. 1, 2019, pp. 53–67. https://doi.org/10.2514/1.C034932.

[4] Walker, E. L., Hemsch, M. J., and West IV, T. K., "Integrated Uncertainty Quantification for Risk and Resource Management: Building Confidence in Design (Invited)," AIAA Paper 2015-0501, January 2015. https://doi.org/10.2514/6.2015-0501.

[5] Nikbay, M., Stanford, B., West IV, T. K., and Rallabhandi, S. K., "Impact of Aeroelastic Uncertainties on the Sonic Boom Signature of a Commercial Supersonic Transport Configuration," AIAA Paper 2017-0040, January 2017. https://doi.org/10.2514/6.2017-0040.

[6] Phillips, B. D., and West IV, T. K., "Aeroelastic Uncertainty Quantification of a Low-Boom Aircraft Configuration," AIAA Paper 2018-0333, January 2018. https://doi.org/10.2514/6.2018-0333.

[7] West IV, T. K., and Phillips, B. D., "Multifidelity Uncertainty Quantification of a Commercial Supersonic Transport," AIAA Paper 2018-2851, June 2018. https://doi.org/10.2514/1.C035496.

[8] West IV, T. K., and Gumbert, C., "Multifidelity, Multidisciplinary Design Under Uncertainty with Non-Intrusive Polynomial Chaos," AIAA Paper 2017-1936, January 2017. https://doi.org/10.2514/6.2017-1936.

[9] Phillips, B. D., Heath, C., and Schmidt, J. N., "System-Level Impact of Propulsive Uncertainties for Low-Boom Aircraft Concepts," AIAA Paper 2020-2730, June 2020. https://doi.org/10.2514/6.2020-2730.

[10] Stevens, S. S., "Perceived Level of Noise by Mark VII and Decibels (E)," *The Journal of the Acoustical Society of America*, Vol. 51, No. 2B, 1972, pp. 575–601. https://doi.org/10.1121/1.1912880.

[11] Rallabhandi, S. K., "Advanced Sonic Boom Prediction Using the Augmented Burgers Equation," *Journal of Aircraft*, Vol. 48, No. 4, 2011, pp. 1245–1253. https://doi.org/10.2514/1.C031248.

[12] Aftosmis, M. J., Nemec, M., and Cliff, S. E., "Adjoint-Based Low-Boom Design with Cart3D," AIAA Paper 2011-3500, June 2011. https://doi.org/10.2514/6.2011-3500.

[13] Pinier, J. T., "Asymmetric Uncertainty Expression for High Gradient Aerodynamics," AIAA Paper 2012-0081, January 2012. https://doi.org/10.2514/6.2012-81.

[14] Park, M. A., and Nemec, M., "Nearfield Summary and Statistical Analysis of the Second AIAA Sonic Boom Prediction Workshop," *Journal of Aircraft*, Vol. 56, No. 3, 2019, pp. 851–875. https://doi.org/10.2514/1.c034866.

[15] Anderson, W. K., Biedron, R. T., Carlson, J.-R., Derlaga, J. M., Druyor, C. T., Gnoffo, P. A., Hammond, D. P., Jacobson, K. E., Jones, W. T., Kleb, B., Lee-Rausch, E. M., Nastac, G. C., Nielsen, E. J., Park, M. A., Rumsey, C. L., Thomas, J. L., Thompson, K. B., Walden, A. C., Wang, L., Wood, S. L., Wood, W. A., Diskin, B., Liu, Y., and Zhang, X., "FUN3D Manual: 14.0," December 2022. URL https://ntrs.nasa.gov/citations/20220017743.

[16] Park, M. A., "Low Boom Configuration Analysis with FUN3D Adjoint Solution Framework," AIAA Paper 2011-3337, June 2011. https://doi.org/10.2514/6.2011-3337.

[17] Rallabhandi, S. K., and Park, M. A., "Adjoint-Based Mesh Adaptation for the Sonic Boom Signature Loudness," AIAA Paper 2017-3049, June 2017. https://doi.org/10.2514/6.2017-3049.

[18] Roe, P. L., "Approximate Riemann Solvers, Parameters Vectors and Difference Schemes," *Journal of Computational Physics*, Vol. 43, No. 2, 1981, pp. 357–372. https://doi.org/10.1006/jcph.1997.5705.

[19] Spalart, P. R., and Allmaras, S. R., "A One Equation Turbulence Model for Aerodynamic Flows," AIAA Paper 92-0439, January 1992. https://doi.org/10.2514/6.1992-439.

[20] "MSC NASTRAN," Online, Retrieved May 10, 2021. URL https://www.mscsoftware.com/product/msc-nastran.

[21] Kiviaho, J. F., Jacobson, K. E., Smith, M. J., and Kennedy, G. J., "A Robust and Flexible Coupling Framework for Aeroelastic Analysis and Optimization," AIAA Paper 2017-4144, June 2017. https://doi.org/10.2514/6.2017-4144.

[22] Saad, Y., and Schultz, M. H., "GMRES: A Generalized Minimum Residual Algorithm for Solving Nonsymmetric Linear Systems," *SIAM Journal of Scientific and Statistical Computing*, Vol. 7, 1986, pp. 856–869. https://doi.org/10.1137/0907058.

[23] Lonzaga, J. B., Page, J. A., Downs, R. S., Kaye, S. R., Shumway, M. J., Loubeau, A., and Doebler, W. J., "PCBoom Version 7 Technical Reference," NASA/TM–20220007177, December 2022. URL https://ntrs.nasa.gov/citations/20220007177.

[24] Loubeau, A., "Review of Noise Metric Sensitivities for Analysis of Quiet Supersonic Overflight," June 2022. URL https://ntrs.nasa.gov/citations/20220009059.

[25] Oberkampf, W. L., and Roy, C. J., *Verification and Validation in Scientific Computing*, Cambridge University Press, Cambridge, 2010. https://doi.org/10.1017/CBO9780511760396.

[26] Eldred, M., and Swiler, L., "Efficient Algorithms for Mixed Aleatory-Epistemic Uncertainty Quantification with Application to Radiation-Hardened Electronics; Part I: Algorithms and Benchmark Results," Tech. Rep. SAND2009-5805, Sandia National Laboratories, September 2009. https://doi.org/10.2172/972887.

[27] Hosder, S., Walters, R. W., and Balch, M., "Point-Collocation Nonintrusive Polynomial Chaos Method for Stochastic Computational Fluid Dynamics," *AIAA Journal*, Vol. 48, No. 12, 2010, pp. 2721–2730. https://doi.org/10.2514/1.39389.

[28] Xiu, D., and Karniadakis, G. E., "The Wiener–Askey Polynomial Chaos for Stochastic Differential Equations," *SIAM Journal on Scientific Computing*, Vol. 24, No. 2, 2002, pp. 619–644. https://doi.org/10.1137/S1064827501387826.

[29] Ghanem, R. G., and Spanos, P. D., *Stochastic Finite Elements: A Spectral Approach*, Springer-Verlag, New York, 1991. https://doi.org/10.1007/978-1-4612-3094-6.

[30] Eldred, M. S., "Recent Advances in Non-Intrusive Polynomial Chaos and Stochastic Collocation Methods for Uncertainty Analysis and Design," AIAA Paper 2009-2274, May 2009. https://doi.org/10.2514/6.2009-2274.

[31] Sudret, B., "Global Sensitivity Analysis Using Polynomial Chaos Expansion," *Reliability Engineering and System Safety*, Vol. 93, No. 7, 2008, pp. 964–979. https://doi.org/10.1016/j.ress.2007.04.002.

[32] Montgomery, D. C., and Runger, G. C., *Applied Statistics and Probability for Engineers*, John Wiley & Sons, Hoboken, 2010.

[33] Phillips, B. D., and Schmidt, J. N., "UQPCE," https://github.com/nasa/UQPCE, 2022.

[34] Sobol, I., "Global sensitivity indices for nonlinear mathematical models and their Monte Carlo estimates," *Mathematics and Computers in Simulation*, Vol. 55, No. 1-3, 2001, pp. 271–280. https://doi.org/10.1016/S0378-4754(00)00270-6.

[35] Saltelli, A., Annoni, P., Azzini, I., Campolongo, F., Ratto, M., and Tarantola, S., "Variance based sensitivity analysis of model output. Design and estimator for the total sensitivity index," *Computer Physics Communications*, Vol. 181, No. 2, 2010, pp. 259–270. https://doi.org/10.1016/j.cpc.2009.09.018.

[36] Rallabhandi, S. K., "Application of Adjoint Methodology to Supersonic Aircraft Design Using Reversed Equivalent Areas," AIAA Paper 2013-2663, San Diego, CA, June 2013. https://doi.org/10.2514/6.2013-2663.

[37] Ordaz, I., Wintzer, M., and Rallabhandi, S. K., "Full-Carpet Design of a Low-Boom Demonstrator Concept," AIAA Paper 2015-2261, June 2015. https://doi.org/10.2514/6.2015-2261.

[38] Wintzer, M., and Ordaz, I., "Under-Track CFD-Based Shape Optimization for a Low-Boom Demonstrator Concept," AIAA Paper 2015-2260, June 2015. https://doi.org/10.2514/6.2015-2260.

[39] McDonald, R. A., and Gloudemans, J. R., "Open Vehicle Sketch Pad: An Open Source Parametric Geometry and Analysis Tool for Conceptual Aircraft Design," AIAA Paper 2022-0004, January 2022. https://doi.org/10.2514/6.2022-0004.

[40] "MSC PATRAN," Online, Retrieved May 10, 2021. URL https://www.mscsoftware.com/product/patran.

[41] "Heldenmesh," Online, Retrieved Oct 26, 2022. URL http://www.heldenaero.com/heldenmesh/.